Applied Surface Science 624 (2023) 157106

Contents lists available at ScienceDirect

Applied Surface Science

journal homepage: www.elsevier.com/locate/apsusc

Full Length Article

# 3D reduced graphene oxide wrapped $MoS_2$@$Sb_2S_3$ heterostructures for high performance sodium-ion batteries

Ming Zhu [a], Jialun Li [a], Xijia Yang [a], Xuesong Li [a], Liying Wang [a,b,*], Wei Lü [a,c,*]

[a] State Key Laboratory of Advanced Structural Materials, Ministry of Education, Changchun University of Technology, Changchun 130012, China
[b] State Key Laboratory of Superhard Materials, Jilin University, Changchun 130012, China
[c] State Key Laboratory of Luminescence and Applications, Changchun Institute of Optics, Fine Mechanics and Physics, Chinese Academy of Sciences, Changchun 130033, China

ARTICLE INFO

*Keywords:*
Sodium-ion battery
Anode materials
Discharge specific capacity
Cyclic stability
Rate performance

ABSTRACT

Metal sulfides have been widely used as the anode materials of sodium-ion batteries (SIBs) due to their high theoretical capacity. However, their inherent low conductivity and irreversible volume expansion limit their electrochemical performance and application. To solve these problems, the $MoS_2$@$Sb_2S_3$ heterostructure composites wrapped by 3D interconnected reduce graphene oxide (rGO) are prepared. The $MoS_2$@$Sb_2S_3$ heterostructure accelerates the transfer of ions and electrons, and provides rich active sites, which facilitates electrolyte penetration and improves the interfacial reaction kinetics. Wrap 3D interconnected rGO networks around the porous $MoS_2$@$Sb_2S_3$ composites to reduce the volume expansion of composite materials in the process of sodiumization and desodiumization, and ensure the structural stability. The theoretical calculation further supports the experimental results that the $MoS_2$@$Sb_2S_3$/rGO heterojunction promotes the redistribution of different charge density and optimizes the adsorption energy of the composite for $Na^+$, thus accelerating the electrochemical reaction kinetics. The $MoS_2$@$Sb_2S_3$/rGO composite as the anode materials of SIBs can achieve a discharge specific capacity of 591.6 mAh $g^{-1}$ at the second cycle with current density of 5 A $g^{-1}$, and 162.1 mAh $g^{-1}$ after 1100 cycles. High-rate capacities are achieved for SIBs (350.4 mAh $g^{-1}$ @ 1 A $g^{-1}$, 260.1 mAh $g^{-1}$ @ 5 A $g^{-1)}$. This work provides a practical method for preparing anode materials of SIBs with excellent electrochemical performance.

## 1. Introduction

Lithium-ion batteries (LIBs) have developed rapidly in recent years due to their high specific energy and excellent cycle performance. However, their large-scale application in electric energy storage is limited due to low natural abundance and uneven geographical distribution of Li [1–3]. Green, clean, low-cost, high-capacity rechargeable batteries are still highly desired [4–6]. Due to its abundant natural reserves, modest cost and electrochemical characteristics similar to those of LIBs, sodium-ion batteries (SIBs) could be the perfect substitute for LIBs [7,8]. However, traditional commercial graphite as anode material of SIB shows dissatisfied specific capacity, and it has been widely used as anode material of LIBs and has achieved great success. The major factor is that ionic radius of $Na^+$ is much larger than that of $Li^+$, and it is difficult to insert the graphite lattice during sodiumization or desodiumization, resulting in huge volume expansion [9,10]. Therefore, finding anode materials with excellent sodium storage capacity and high structural stability is crucial for commercialization of SIBs.

At present, layered metal sulfide $MS_x$ (M = Mo, Sb, Sn, Bi, etc.) has been widely studied as SIB anode material, mainly due to its high theoretical capacity [11–14]. As a feasible anode material for SIB, the theoretical capacity of $Sb_2S_3$ is 946 mAh $g^{-1}$. However, the huge volume expansion and poor ionic conductivity of $Sb_2S_3$ during charging and discharging lead to low specific capacity, poor cycling stability and low cycle life [15–18]. In order to solve these problems, heterostructure composites composed of two different metal sulfides have been widely studied [19–22]. By chemical vapor deposition technology, Fang *et al.* synthesized $Sb_2S_3$/$SnS_2$ heterostructure exhibiting impeccable rate performance in SIBs [23]. Li *et al.* synthesized nitrogen-doped carbon-coated $CoS_2$/$Sb_2S_3$ core/shell heterostructure, whose unique carbon-

* Corresponding authors at: State Key Laboratory of Advanced Structural Materials, Ministry of Education, Changchun University of Technology, Changchun 130012, China.
*E-mail addresses:* wangliying@ccut.edu.cn (L. Wang), lvwei@ccut.edu.cn (W. Lü).

https://doi.org/10.1016/j.apsusc.2023.157106
Received 15 December 2022; Received in revised form 19 January 2023; Accepted 20 March 2023
Available online 24 March 2023

coated heterostructure brought long cycle life [24]. Heterostructure can improve the interfacial reaction kinetics, accelerate the diffusion of ions and electrons, and thus improve the conductivity and electrochemical performance of electrode materials [25]. Meanwhile, the bimetallic sulfide also provides more redox sites and lower optical binding gap [26,27].

The combination of metal sulfide and carbon matrix is also one of the important strategies to solve the above problems. In general, simple carbon coating could effectively reduce the interface resistance, increase the electrical conductivity and improve the electrochemical performance of materials [28]. However, the large radius of $Na^+$ may still cause the cracking of carbon layer during desodiumization and sodiumization, thus reducing the electrochemical performance [29]. Recently, 3D interconnected reduced graphene oxide (rGO) network, as the electrode material of SIBs, has received great attention owing to its outstanding mechanical ductility, excellent electronic conductivity and significant specific surface area [30,31]. Zhang *et al.* reported SnSb nanoparticle-anchored N-doped 3D rGO as anode of SIBs, and the first cycle discharge specific capacity reached 1169 mAh $g^{-1}$ at 0.1C [32]. Cao *et al.* fabricated $Sb_2S_3$@$FeS_2$/N-rGO hollow nanorods by a two-step solvothermal method, with a high-capacity retention rate of 85.7 % after 1000 cycles at 5 A $g^{-1}$ [33]. Zhao et al. reported a new design of $SnO_2$@$SnS_2$ heterostructured quantum dots anchored on nitrogen-doped graphene ($SnO_2$@$SnS_2$@NG), used for SIBs anode materials to exhibit superstrong ion diffusion kinetics and excellent sodium storage performance [34]. The 3D interconnected rGO network promotes the electrolyte penetration and ion shuttle process, thereby greatly improving the sodium storage performance [35].

Based on above discussion, bimetallic sulfides coated with 3D interconnected rGO network may be a promising way to achieve high-performance SIBs, but the Sb-based anode material family still needs further exploration. In this work, $MoS_2$@$Sb_2S_3$/rGO composite heterostructures are fabricated by hydrothermal vulcanization method. In the composite, 3D interconnected rGO is used as a support template to enhance conductivity and specific surface area, and cushion the volume expansion during charging and discharging. At the same time, the new design of the three-dimensional interconnected conductive skeleton structure greatly shortens the $Na^+$ diffusion path and increases the contact area between the electrolyte and the active material. The interface between $Sb_2S_3$ and $MoS_2$ induces an internal electric field, which promotes $Na^+$ pumping into the interface, greatly reduces the activation barrier and improves the kinetics of the entire material conversion reaction. In addition, the different redox potentials of $Sb_2S_3$ and $MoS_2$ also alleviate the volume expansion during the sodiumization and desodiumization, and ensure the structural stability of the composite. As a result, the excellent performance of SIBs based on $MoS_2$@$Sb_2S_3$/rGO anode is achieved.

## 2. Experiment

### 2.1. Synthesis of $Sb_2MoO_6$/rGO

Graphene oxide (GO) was produced by a modified Hummers method [36]. $Sb_2MoO_6$/rGO was prepared by one-step hydrothermal method. Typically, 0.62 g ammonium molybdate tetrahydrate was dissolved in 25 ml of GO aqueous solution under stirring. Then, 0.456 g antimony trichloride was dissolved in 10 ml absolute ethanol. Mixing the two solutions thoroughly until it turns to dark green. Finally, the mixed solution was transferred into a 50 ml Teflon-lined reactor and kept at 160 °C for 36 h. Powder samples were obtained after washing and freeze-drying.

### 2.2. Synthesis of $MoS_2$@$Sb_2S_3$/rGO

The $MoS_2$@$Sb_2S_3$/rGO heterostructures were fabricated by high temperature vulcanization in $N_2$ atmosphere. At first, 0.2 g $Sb_2MoO_6$/rGO and 0.6 g of sulfur powder were mixed and put in the center of a tube furnace, which is kept at 500 °C for 2 h in $N_2$. After cooling, the black $MoS_2$@$Sb_2S_3$/rGO powder sample was acquired. For comparison, $MoS_2$@$Sb_2S_3$ was also produced using the same technique without the addition of GO.

### 2.3. Material characterization

The samples were characterized by X-ray diffraction (XRD, D/max-2500 PC X-ray diffractometer), field emission scanning electron microscopy (FESEM, S4800, Hitachi Corporation), transmission electron microscopy (TEM, FEI Talos F200), X-ray photoelectron spectroscopy (XPS, Thermo Scientific, Waltham, MA, USA), and Raman spectrometer (Raman, HR-Evolution). The Brunauer-Emmett-Teller (BET) specific surface area and pore size distribution of the samples were determined by $N_2$ adsorption/desorption (NOVA 2000, Quanta chrome).

### 2.4. Electrochemical characterization

In an argon glove box, the $MoS_2$@$Sb_2S_3$/rGO electrode was assembled into a CR2032 coin cell. The working electrode was consisted of $MoS_2$@$Sb_2S_3$/rGO-based active material (70 wt%), conductive carbon black (20 wt%), and sodium carboxymethyl cellulose (CMC, 10 wt%). Use an appropriate amount of deionized water as the stirring solvent, grind for 1 h, and coat the slurry on the copper foil. After the copper foil was dried in a vacuum oven at 60 °C, it was cut into round pieces with a diameter of 1.2 cm, and the active substance load of each piece was between 1.2 and 1.5 mg $cm^{-2}$. The positive electrode is metal sodium sheet, and the separator is glass fiber membrane (Whatman, GF/D). 1 M $NaClO_4$ was added to ethylene carbonate/diethyl carbonate (1:1, V/V) as the electrolyte. The galvanostatic charge–discharge (GCD) performance in the voltage range of 0.01–3 V was tested by the blue electricity test system (LAND CT2001A). Cyclic voltammetry (CV) curves were measured in the 0–3 V voltage range at a scan rate of 0.1 mV $s^{-1}$. Electrochemical impedance spectroscopy (EIS) spectra were recorded at the frequency range of 0.01 HZ to 100 KHZ. Both of CV and EIS were test on CHI660E electrochemical workstation (Shanghai Chenhua Instrument Co., Ltd.).

### 2.5. Computational method

The Materials Studio was employed in the DFT calculation. The Perdew-Wang (PWC) version of the local density approximation (LDA) was applied for the exchange and correlation. The kinetic energy cutoff of 450 eV was adopted for the wave function expansion. Moreover, Brillouin zone integration on the grid with a 2 × 2 × 1 k-grid mesh was performed for geometry optimization and calculation of density of states. A 13 Å vacuum layer thickness was applied to avoid virtual interaction. The $MoS_2$@$Sb_2S_3$ and $MoS_2$@$Sb_2S_3$/rGO composites were assessed to reveal their structural and electronic properties. The corrected adsorption energy of $Sb_2S_3$, $MoS_2$@$Sb_2S_3$ or $MoS_2$@$Sb_2S_3$/rGO ($\Delta E_{ads}$) was defined as.

$\Delta E_{ads} = E_{total} - E_{host} - E_{guest} - E^{+}_{Na}$.

where $E_{total}$ is the total energy of $Sb_2S_3$, $MoS_2$@$Sb_2S_3$ or $MoS_2$@$Sb_2S_3$/rGO surface adsorbed with $Na^+$, while $E_{host}$ and $E_{guest}$ are the total energy of $Sb_2S_3$, $MoS_2$@$Sb_2S_3$ or $MoS_2$@$Sb_2S_3$/rGO and solo $Na^+$, respectively.

## 3. Results and discussion

The synthesis process of $MoS_2$@$Sb_2S_3$/rGO is shown in Fig. 1. At first, the nanosheet-like $Sb_2MoO_6$/rGO precursor was synthesized by hydrothermal and freeze-drying processes. Subsequently, the $Sb_2MoO_6$/rGO precursor was subjected to a high-temperature vulcanization process in $N_2$ atmosphere to obtain a porous sheet-like $MoS_2$@$Sb_2S_3$/rGO heterostructure. The freeze-dried rGO nanosheets were transformed into

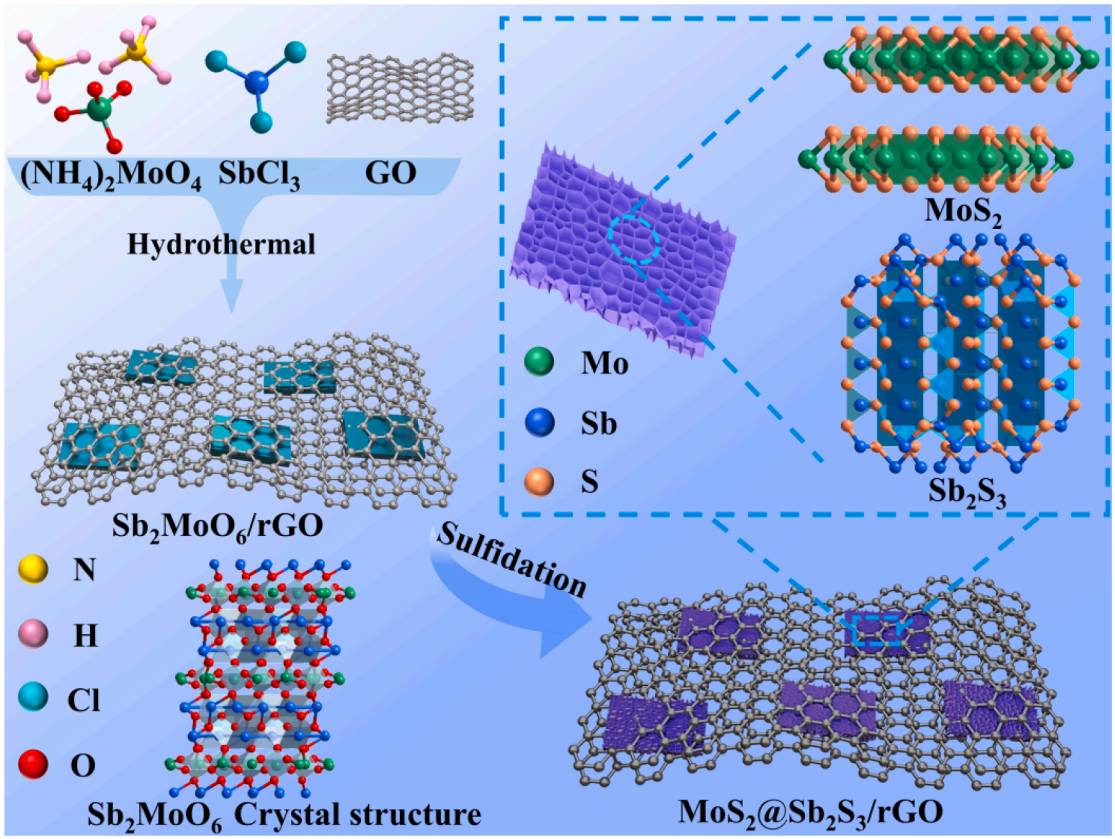


**Fig. 1.** Schematic illustration of the synthesis process of $MoS_2@Sb_2S_3$/rGO.

porous 3D internet-like structures, which completely covered on the surface of the $MoS_2@Sb_2S_3$ composite. Therefore, the as-prepared $MoS_2@Sb_2S_3$/rGO porous nanosheets is expected to have larger specific surface area, high electrical conductivity and fast ion transport channels.

The morphologies of $Sb_2MoO_6$/rGO, $MoS_2@Sb_2S_3$ and $MoS_2@Sb_2S_3$/rGO were observed by SEM. As shown in Fig. S1, $Sb_2MoO_6$/rGO exhibits nanosheet morphology, and the average size is ~ 7 μm. The surface is smooth, and the elemental mapping indicates the uniform distribution of O, Mo, Sb on rGO sheets. As shown in Fig. 2a, the size of the $MoS_2@Sb_2S_3$/rGO nanosheets has not changed, and most of the nanosheets are embedded in the three-dimensional graphene network, forming a three-dimensional interconnected conductive framework structure. The high-magnification SEM image of $MoS_2@Sb_2S_3$/rGO nanosheets is shown in Fig. 2b. It can also be seen that $MoS_2@Sb_2S_3$/rGO nanosheets are wrapped by graphene networks. The inset shows that the nanosheets surface presents a porous and wrinkled structure. The origination of porous wrinkled structure is probably due to the $MoS_2$ nanosheets generated by reorganizing binary metal oxides into metal sulfides at the lattice level during high-temperature sulfidation. The porous wrinkled network facilitates sufficient wetting between the electrolyte and active material, which could greatly facilitate $Na^+$ intercalation and deintercalation, and improve the reversibility of the material. As shown in Fig. S2(a, b), the size of $MoS_2@Sb_2S_3$ composite without adding GO is slightly reduced with similar porous structure, showing a nano-block structure with a length of 3–4 μm. Fig. S3 shows the SEM image of pure graphene oxide, it can be seen that graphene presents a three-dimensional network structure. It facilitates the anchoring effect of the $MoS_2@Sb_2S_3$ heterojunction, which is beneficial to buffer the huge volume expansion of the $MoS_2@Sb_2S_3$/rGO composite during the charge–discharge process.

From the TEM image in Fig. 2(c, d), it can be further observed that the $MoS_2@Sb_2S_3$/rGO composite is composed of many ultrathin nanosheets with a large number of holes on the surface, $MoS_2@Sb_2S_3$ nanosheets are all embedded in the three-dimensional interconnected rGO, presenting a three-dimensional conductive framework structure, and this greatly increases the specific surface area of the composite material and facilitates the penetration process of the electrolyte into the material. Fig. 2d is the HRTEM image of $MoS_2@Sb_2S_3$/rGO. The lattice spacing of 0.615 nm corresponds to the (002) crystal plane of $MoS_2$ (JCPDS: 24-0513). The lattice spacing of 0.565 nm is assigned to the (200) crystal plane of $Sb_2S_3$ (JCPDS: 73-0393), and the clear boundary between them proves the successful construction of the $MoS_2@Sb_2S_3$ heterojunction. Fig. 2e is the element mapping of $MoS_2@Sb_2S_3$/rGO, which verifies that Sb, Mo, and S elements are uniformly distributed in the composite. The elemental mapping of $MoS_2@Sb_2S_3$ are shown in Fig. S2c.

The elemental composition of the samples was accurately determined by XRD. In Fig. S4a, all the diffraction peaks of $Sb_2MoO_6$/rGO correspond to the XRD card (JCPDS NO. 26-0107) of the triclinic structure $Sb_2MoO_6$. Fig. 3a is the XRD pattern of $MoS_2@Sb_2S_3$/rGO composite, there are three diffraction peaks at 14.3°, 33.4°, and 39.5°, which belong to the the (002), (101) and (103) crystal planes of $MoS_2$ (JCPDS: 24-0513), respectively. The diffraction peaks at 17.5°, 24.9°, 29.2°, and 32.3° correspond to the (201), (103), (211) and (212) characteristic surfaces of $Sb_2S_3$ (JCPDS: 73-0393), respectively. The XRD pattern of $MoS_2@Sb_2S_3$ was also analyzed in Fig. S4b, and all diffraction peaks detected correspond exactly to standard cards of $MoS_2$ (JCPDS: 24-0513) and $Sb_2S_3$ (JCPDS NO. 26-0107), which proves the successful synthesis of $MoS_2@Sb_2S_3$.

$MoS_2@Sb_2S_3$/rGO bonds and valence states were measured by XPS. The survey spectrum in Fig. 3b shows that $MoS_2@Sb_2S_3$/rGO contains the elements Sb, Mo, S, and C. The high-resolution Sb 3d XPS spectrum of the $MoS_2@Sb_2S_3$/rGO composite split into two spin–orbit doublet states in Fig. 3c. The peaks at 539.1 eV and 540 eV can be connected to the Sb $3d_{3/2}$ state, and the peaks at 529.6 and 530.4 eV can be ascribed

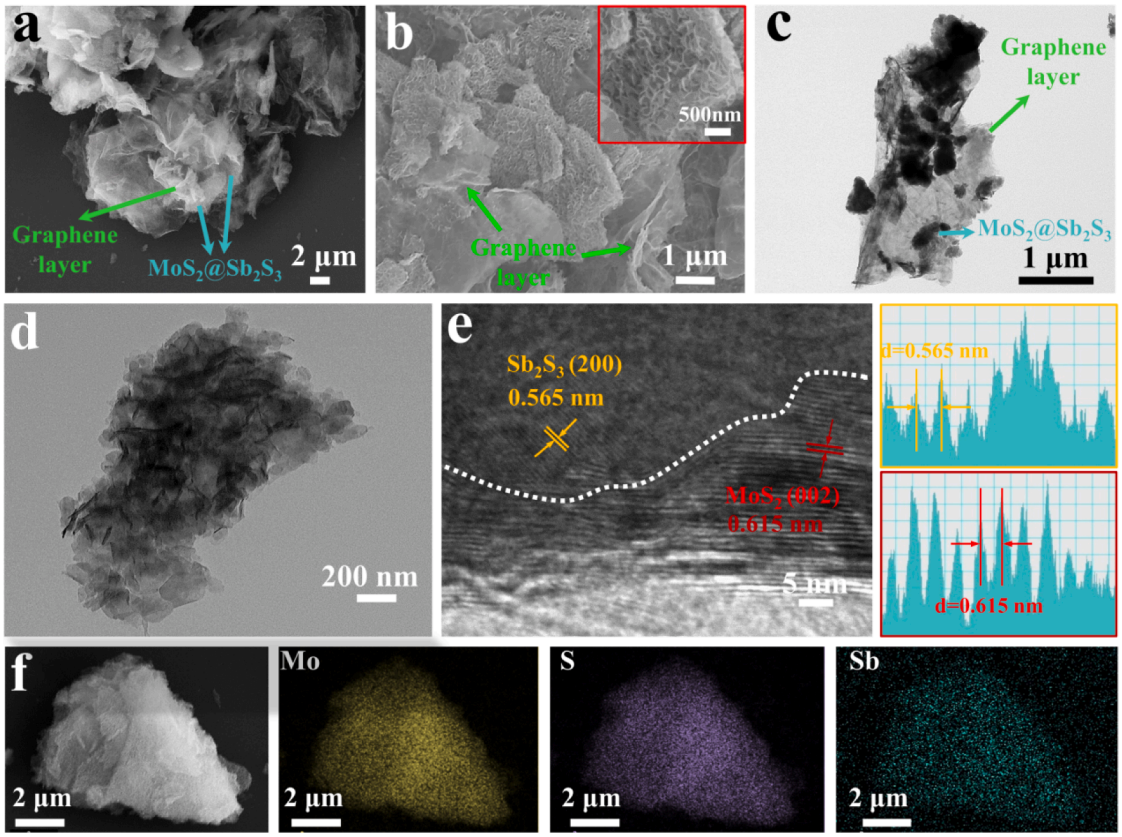


**Fig. 2.** (a) Low magnification SEM images of $MoS_2@Sb_2S_3$/rGO. (b) High magnification SEM images of $MoS_2@Sb_2S_3$/rGO, the inset is a partial enlarged view of $MoS_2@Sb_2S_3$/rGO nanosheets. (c, d) TEM image of $MoS_2@Sb_2S_3$/rGO. (e) HRTEM image of $MoS_2@Sb_2S_3$/rGO and the corresponding lattice spacing profile. (f) element mapping of $MoS_2@Sb_2S_3$/rGO.

with the Sb $3d_{5/2}$ state [37], the photoelectron peaks at $MoS_2@Sb_2S_3$/rGO at 531.6 eV and $MoS_2@Sb_2S_3$ at 533.1 eV both belong to O 1s, which may be caused by partial absorption of oxygen and water when the sample is exposed to air. Compared with the $MoS_2@Sb_2S_3$ material, each peak in the Sb 3d spectrum (Fig. 3c), Mo 3d spectrum (Fig. 3d) and S 2p spectrum (Fig. 3e) of $MoS_2@Sb_2S_3$/rGO composites shift to lower binding energies, this result confirms the electronic coupling effect between $MoS_2@Sb_2S_3$ and 3D interconnected rGO, in which electrons transfer rapidly. In Fig. 3d, the Mo 3d peaks of the $MoS_2@Sb_2S_3$/rGO composite appeared at 232.4 eV (Mo $3d_{3/2}$) and 229.3 eV (Mo $5d_{3/2}$), compared with the $MoS_2@Sb_2S_3$ spectra (232.7 eV and 229.6 eV), moving to lower binding energy, the characteristic peak intensities are also smaller, indicating that rGO masks the peak intensities of the $MoS_2$ and $Sb_2S_3$ components [38]. As shown in Fig. 3e, in the $MoS_2@Sb_2S_3$@rGO composite, the sulfur peaks at 162.2 eV and 163.4 eV were ascribed to the S $2p_{3/2}$ and S $2p_{1/2}$ orbitals of S 2p, respectively, proving that the sulfurization was successful. Fig. 3f is the high-resolution C 1s XPS spectrum of $MoS_2@Sb_2S_3$/rGO, two peaks at 284.8 eV and 286.3 eV in the C 1s spectra are closely correlated with the C—C/C=C and C—O bonds, respectively [39]. The total spectrum of $MoS_2@Sb_2S_3$ is also given in Fig. S6a, Supporting Information, and Mo, Sb, and S elements are detected. The high-resolution XPS spectra of $Sb_2MoO_6$/rGO are analyzed in detail in Fig. S6, Supporting Information.

Fig. 3g and Fig. S7 present the Raman spectra of $MoS_2@Sb_2S_3$@rGO and $Sb_2MoO_6$/rGO, respectively. Two strong peaks were observed around 1340 and 1580 $cm^{-1}$ for both composites, corresponding to D band and G band, respectively, confirming the existence of rGO. In Fig. 3g, the small characteristic peak at 100–300 $cm^{-1}$ belongs to $Sb_2S_3$, and the $MoS_2$ in-plane $E^1_{2g}$ and out-of-plane $A_{1g}$ vibrations are represented by the two sharp peaks at 378 and 403 $cm^{-1}$, respectively, confirmed the successful formation of $MoS_2@Sb_2S_3$ heterojunction. In Fig. S7, the two peaks at 716 and 812 $cm^{-1}$ are ascribed to $Sb_2MoO_6$. Fig. 3h shows the specific surface area of $MoS_2@Sb_2S_3$/rGO by measured BET method to be 33.1828 $m^2\ g^{-1}$, which is larger than those of $Sb_2MoO_6$/rGO (30.0743 $m^2\ g^{-1}$) and $MoS_2@Sb_2S_3$ (24.6340 $m^2\ g^{-1}$), demonstrating that the introduction of 3D interconnected rGO increased the specific surface area, facilitated electrolyte penetration, and provided more reactive sites for $Na^+$ intercalation. Fig. 3i and Fig. S8 are the pore size distribution diagrams of $MoS_2@Sb_2S_3$/rGO and $MoS_2@Sb_2S_3$, respectively, and the measured average pore sizes of $MoS_2@Sb_2S_3$/rGO and $MoS_2@Sb_2S_3$ are 8.1314 nm and 9.658 nm, respectively.

In order to explore the reduction–oxidation behavior of $MoS_2@Sb_2S_3$/rGO during sodium storage, we performed CV tests. In Fig. 4a, the first broad peak appears around 1.25 V during the first discharge, indicating that $Na^+$ intercalate into the $MoS_2$ lattice [40]. A reduction peak appeared around 0.87 V and disappeared in subsequent scans, it was proved that the solid electrolyte interface (SEI) film was formed. The two reduction peaks at 0.68 V and 0.4 V correspond to the transformation of $Sb_2S_3$ components and the further alloying of $Sb^0$ to form by-products, respectively [41]. The sharp peak at 0.01 V is attributed to the formation of $Na_xMoS_2$ [42]. The $Na_xMoS_2$ and Mo phases formed during the discharge process can both reduce the volume expansion when the $Sb_2S_3$ components are converted to $Sb^0$ and $Na_3Sb$, thereby ensuring the structural stability of the $MoS_2@Sb_2S_3$/rGO composite [43]. During the first charge, the oxidation peaks at 0.75 V and 1.3 V are assigned to the reverse transformation of $Na_3Sb$ and the formation of $Sb^0$ components, respectively [44]. The broad peaks at 1.84 V and 2.34 V correspond to the process of $Na^+$ extraction to form $MoS_2$ and $Sb_2S_3$ components [45]. In the subsequent second and third scans, the CV curves are highly overlapped, indicating that the composite has superb structural stability and high electrochemical reversibility. The CV curves of $Sb_2MoO_6$/rGO and $MoS_2@Sb_2S_3$ are shown in Fig. S9a, b,

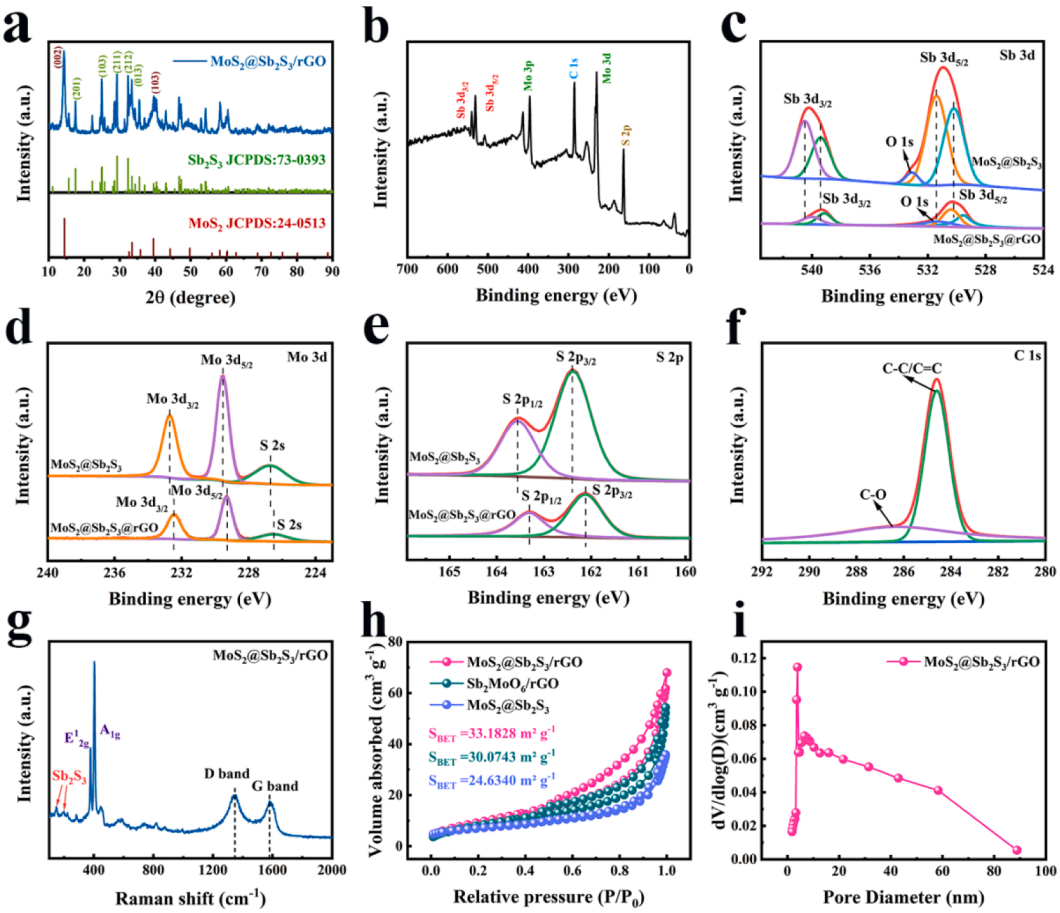


**Fig. 3.** (a) XRD patterns of $MoS_2$@$Sb_2S_3$/rGO. (b) High-resolution XPS Survey spectra of $MoS_2$@$Sb_2S_3$. (c-e) are High-resolution of Sb 3d, Mo 3d and S 2p XPS spectra of $MoS_2$@$Sb_2S_3$ and $MoS_2$@$Sb_2S_3$/rGO composite. (f) High-resolution C 1s XPS spectra of $MoS_2$@$Sb_2S_3$/rGO. (g) Raman spectra of $MoS_2$@$Sb_2S_3$/rGO. (h) $N_2$ adsorption/desorption isotherms. (i) pore size distribution of $MoS_2$@$Sb_2S_3$/rGO.

respectively. The electrochemical reactions of $MoS_2$@$Sb_2S_3$/rGO during sodium storage are as follows:

$$MoS_2 + xNa^+ + xe^- \leftrightarrow Na_xMoS_2 \quad (1)$$

$$Sb_2S_3 + 6Na^+ + 6e^- \leftrightarrow 2Sb^0 + 3Na_2S \quad (2)$$

$$Sb^0 + 3Na^+ + 3e^- \leftrightarrow Na_3Sb \quad (3)$$

$$Na_xMoS_2 + (4 - x)e^- + (4\text{-}x)Na^+ \leftrightarrow Mo + 2Na_2S \quad (4)$$

The GCD curves of $MoS_2$@$Sb_2S_3$/rGO at 0.1 A $g^{-1}$ for the first 5 cycles are shown in Fig. 4b. Generally, the significant capacity loss in the first cycle is attributed to the formation of SEI film. The first discharge capacity is 679 mAh $g^{-1}$ and the charging capacity is 547 mAh $g^{-1}$, corresponding to an initial coulombic efficiency of 80.6 %. The charge–discharge curves of the last four laps almost overlap, indicating that the battery capacity decays slowly. In contrast, as shown in Fig. S10a, the first charge–discharge capacity of $Sb_2MoO_6$/rGO is only 404 mAh $g^{-1}$ and 670 mAh $g^{-1}$, and the initial coulombic efficiency is 60 %. The charge–discharge curve of $MoS_2$@$Sb_2S_3$ is shown in Fig. S10b, the initial charge–discharge capacity is 488 mAh $g^{-1}$ and 601 mAh $g^{-1}$, respectively, and the initial coulomb efficiency is 81 %.

Fig. 4d compares the cycling performance of $MoS_2$@$Sb_2S_3$/rGO, $Sb_2MoO_6$/rGO, and $MoS_2$@$Sb_2S_3$. The $MoS_2$@$Sb_2S_3$/rGO exhibits a second discharge capacity of 618 mAh $g^{-1}$, which can provide a discharge capacity of 380.6 mAh $g^{-1}$ after 100 cycles at 0.1 A $g^{-1}$. In contrast, the capacity of $Sb_2MoO_6$/rGO and $MoS_2$@$Sb_2S_3$ electrode materials decreased significantly, the second discharge capacities are 470 mAh $g^{-1}$ and 502 mAh $g^{-1}$, respectively, and the specific capacities after 100 cycles are 260 mAh $g^{-1}$ and 72 mAh $g^{-1}$, respectively. At the same time, it can be noticed that $Sb_2MoO_6$/rGO exhibits better cycle stability than $MoS_2$@$Sb_2S_3$, which is attributed to the coating of the 3D interconnected rGO network, buffering its volume expansion during the sodium deintercalation process.

The rate performances of $MoS_2$@$Sb_2S_3$/rGO, $Sb_2MoO_6$/rGO, and $MoS_2$@$Sb_2S_3$ are also investigated. As shown in Fig. 4(c, e), the electrode delivers discharge capacities of 678, 486.2, 413.2, 350.4, and 260.1 mAh $g^{-1}$ at 0.1, 0.2, 0.5, 1.0 and 5.0 A $g^{-1}$, respectively. The material's specific capacity was 588.5 mAh $g^{-1}$ when the current density was restored to 0.1 A $g^{-1}$, and the rate performance was basically recovered. In contrast, the $Sb_2MoO_6$/rGO and $MoS_2$@$Sb_2S_3$ anode materials in Fig. S11(a, b) exhibit poor rate performance. At 5 A $g^{-1}$, the discharge specific capacities are only 114 mAh $g^{-1}$ and 166 mAh $g^{-1}$, respectively. When recovered to 0.1 A $g^{-1}$, the discharge specific capacities are 377 mAh $g^{-1}$ and 325 mAh $g^{-1}$, respectively. Fig. 4f is a photo of a sodium-ion battery lighting an LED lamp based on $MoS_2$@$Sb_2S_3$/rGO electrode material.

The long-cycle performance of $MoS_2$@$Sb_2S_3$/rGO anode material at 5 A $g^{-1}$ was further tested. In Fig. 4g, the discharge capacity decreased sharply in the first 50 cycles, possibly due to the protective effect of the SEI film, which resulted in insufficient contact between the electrolyte and the active material, and difficulty in $Na^+$ insertion/extraction. As the electrolyte slowly penetrated into the inside of the active material, the discharge capacity is stable after 200 cycles. The discharge capacity of 162 mAh $g^{-1}$ can still be maintained after 1100 cycles. As shown in the inset of Fig. 4g, $Sb_2MoO_6$/rGO without heterostructure and the $MoS_2$@$Sb_2S_3$ anode material without adding 3D interconnected rGO

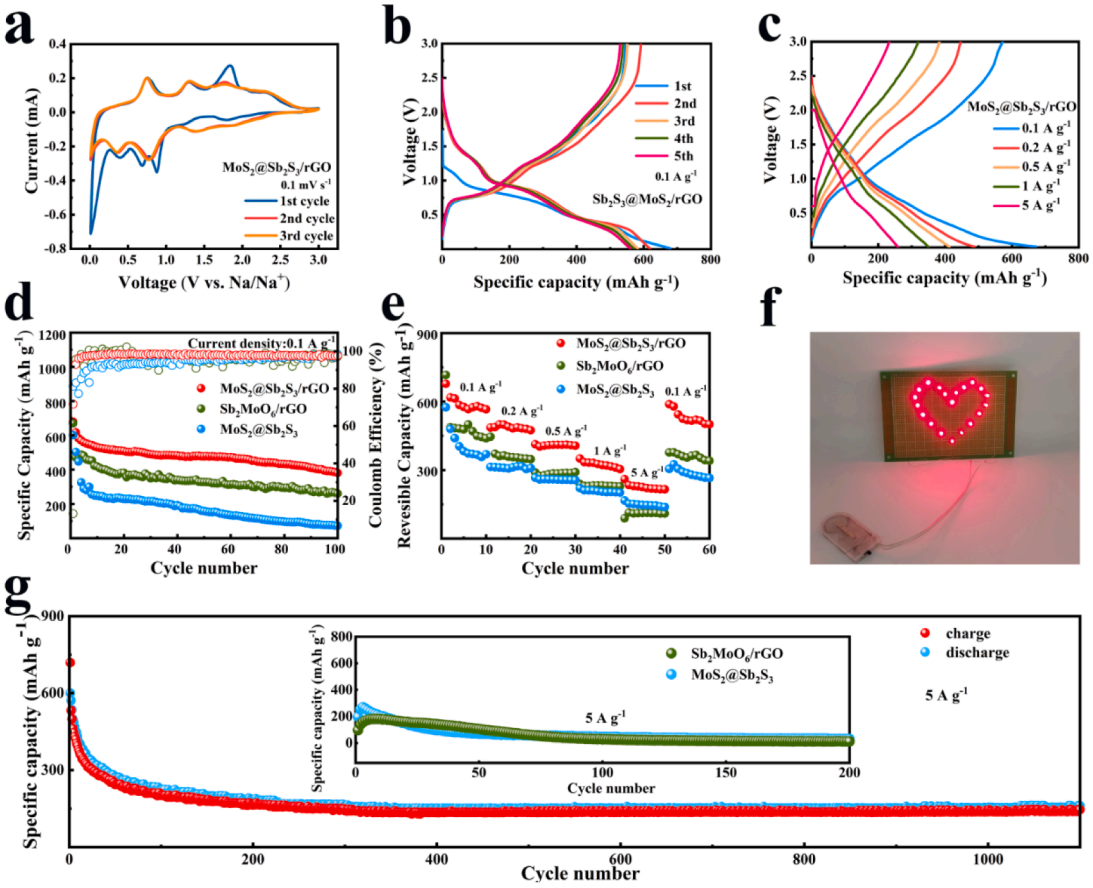


**Fig. 4.** (a) CV curves of $MoS_2@Sb_2S_3$/rGO at a scan rate of 0.1 mV $s^{-1}$ for the first three cycles. (b) GCD curves of $MoS_2@Sb_2S_3$/rGO for the first five cycles at 0.1 A $g^{-1}$. (c) GCD curves of $MoS_2@Sb_2S_3$/rGO at different current densities. (d) Cycling performance and coulombic efficiency of $MoS_2@Sb_2S_3$/rGO, $Sb_2MoO_6$/rGO and $MoS_2@Sb_2S_3$ at 0.1 A $g^{-1}$. (e) Rate capability of $MoS_2@Sb_2S_3$/rGO, $Sb_2MoO_6$/rGO and $MoS_2@Sb_2S_3$ at different current density. (f) Photo of lighting up LED lights. (g) Cycling stability of $MoS_2@Sb_2S_3$/rGO anode at 5 A $g^{-1}$ for 1100 cycles. The inset is the cycle performance diagram of $MoS_2@Sb_2S_3$ and $Sb_2MoO_6$/rGO at 5 A $g^{-1}$.

network will agglomerate and pulverize during the process of sodiumization and desodination, resulting in lower discharge capacity. After 200 cycles at 5 A $g^{-1}$, the discharge capacity almost drops to zero.

It can be thus concluded that $MoS_2@Sb_2S_3$/rGO has high-rate performance and long cycle stability, which is mainly attributed to the formation of a unique heterostructure, and the interfacial energy of the heterointerface reaction and the electrode reaction's kinetics are enhanced. In the process of $Na^+$ intercalation and de-alloying, the formed interphase $Na_xMoS_2$ and Mo elements can effectively limit the volume expansion of the $Sb_2S_3$ component, thereby reducing the pulverization of electrode materials. In addition, the 3D interconnected rGO network also provides a abundant holes and active sites for the material, which facilitates the penetration of the electrolyte and improves the sodium storage performance of the composite [46,47].

The reaction kinetics of $MoS_2@Sb_2S_3$/rGO was further analyzed by comparing the CV curves at various scan speeds. In Fig. 5a, with the increasing scan speeds, the redox peaks shifted in opposite directions with similar profiles, indicating that the charge storage process of $MoS_2@Sb_2S_3$/rGO composites involves diffusion-controlled intercalation and surface capacitance processes [48]. Following is a description of the connection between scan rate (v) and peak current (i) [49]:

$$i = av^b \tag{5}$$

$$\log i = b\log v + \log a \tag{6}$$

Both a and b values can be adjusted. Diffusion control is dominant when b is equal to 0.5, and when the value of b is 1, it is dominated by the surface capacitive process [50]. In Fig. 5b, the b values of the five peaks of the CV curve are all close to 1, indicating that the $MoS_2@Sb_2S_3$/rGO composite is mainly dominated by the surface capacitance contribution, accompanied by a small part of the diffusion-controlled process. Additionally, at a certain scanning speed, the diffusion contribution and the surface capacitance contribution can be calculated by Equation (7) [51]:

$$i = k_1 v + k_2 v^{1/2} \tag{7}$$

$k_1v$ and $k_2v^{1/2}$ represent the surface capacitance contribution and the diffusion contribution, respectively, and can be calculated from equation (7) at each scan speed. Fig. 5c demonstrates that the $MoS_2@Sb_2S_3$/rGO composite has a capacitive control contribution of 94.1 % at 0.5 mV $s^{-1}$, which is greater than that of the $Sb_2MoO_6$/rGO (49.1 %, Fig. S12) and $MoS_2@Sb_2S_3$ (88.2 %, Fig. S13). According to Fig. 5d, the contribution of the $MoS_2@Sb_2S_3$/rGO surface capacitance rises from 77.8 % to 97.3 % when the scan speed increases from 0.1 mV $s^{-1}$ to 1 mV $s^{-1}$. The above results reveal that the sodium storage process of $MoS_2@Sb_2S_3$/rGO composites is mainly dominated by the surface capacitance contribution, this result is mainly due to the formation of a porous sheet-like heterostructure with a unique wrinkle network, which accelerates the penetration of the electrolyte and enhances the $Na^+$ diffusion ability. At the same time, the close contact of p-type $Sb_2S_3$ and n-type $MoS_2$ makes the charge distribution around them non-uniform, which accelerates the transfer of $Na^+$ on the heterointerface.

The reaction kinetics were further analyzed by EIS test. As shown in Fig. 5e, the inset is the equivalent circuit diagram model, each Nyquist curve consists of a semicircle and a slope line. The Warburg impedance (Zw) during $Na^+$ diffusion is shown by the oblique line, and the

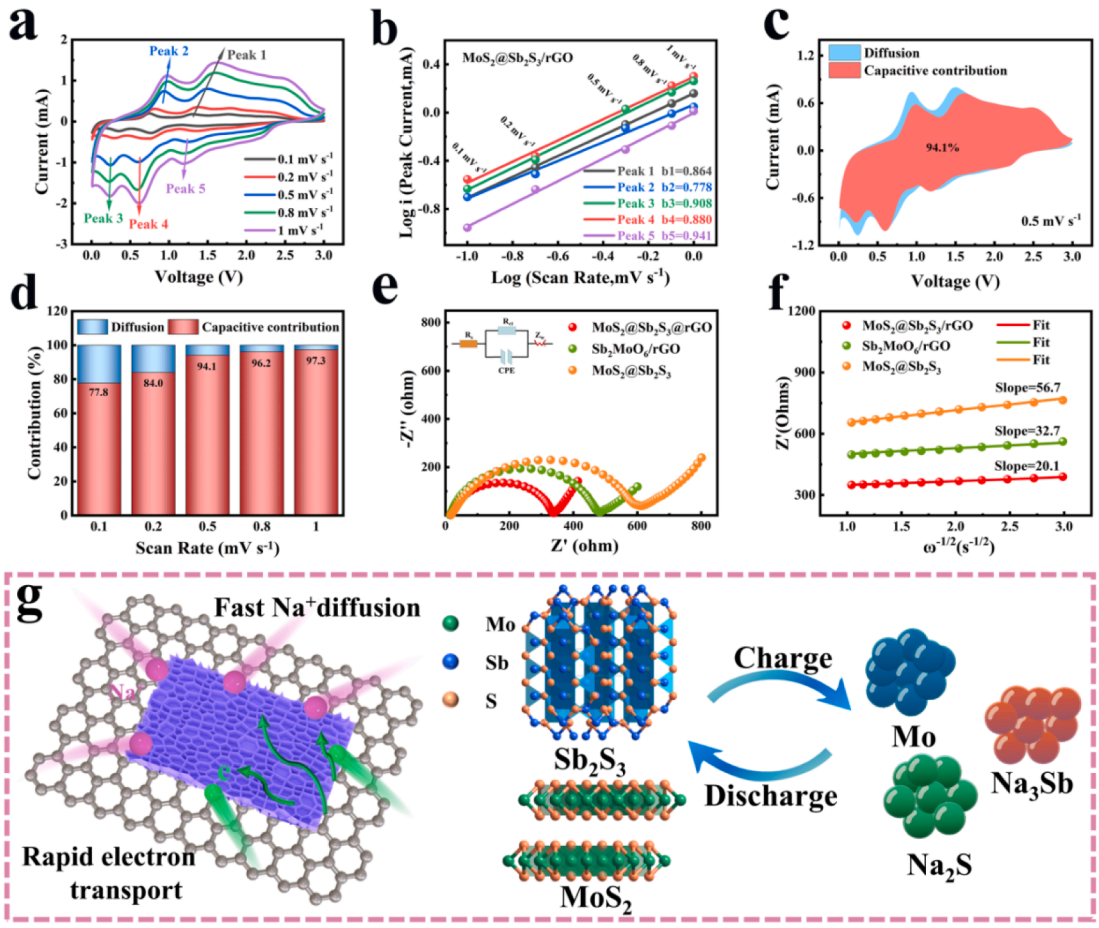


**Fig. 5.** (a) CV curves of $MoS_2@Sb_2S_3$/rGO at scan rates from 0.1 to 1.0 mV $s^{-1}$. (b) Fitting graph of log(i) and log(v) under each peak. (c) Capacitive contributed capacity ratio of $MoS_2@Sb_2S_3$/rGO at 0.5 mV $s^{-1}$. (d) Capacitive contribution ratio of $MoS_2@Sb_2S_3$/rGO at different scan rates. (e) EIS spectra of $MoS_2@Sb_2S_3$/rGO, $Sb_2MoO_6$/rGO, $MoS_2@Sb_2S_3$ and $Sb_2MoO_6$. (f) Relationships between Z' and $\omega^{-1/2}$ in the low frequency range of $MoS_2@Sb_2S_3$/rGO, $Sb_2MoO_6$/rGO and $MoS_2@Sb_2S_3$. (g) Schematic illustration of the sodium storage mechanism.

semicircle's diameter corresponds to the charge transfer impedance (Rct). In Table S1, the charge transfer impedance (316 Ω) of $MoS_2@Sb_2S_3$/rGO is smaller than that of $Sb_2MoO_6$/rGO (457.5 Ω) and that of $MoS_2@Sb_2S_3$ (535.1 Ω), indicating that $MoS_2@Sb_2S_3$/rGO has excellent electrode kinetics. To further explore the $Na^+$ transfer mechanism, the connection between Z' and $\omega^{-1/2}$ was plotted in Fig. 5f. The diffusion rate ($D_{Na}$) of $Na^+$ can be calculated from Equation (8) [52]:

$$D_{Na} = R^2T^2/2A^2n^4F^4C^2\sigma^2 \quad (8)$$

R, T, A, n, F, C, and σ indicate gas constant, absolute temperature, electrode surface area, transmitted electrons per unit mass, Faraday's constant, and Warburg factor, respectively. According to Table S1, the $Na^+$ diffusion coefficient ($D_{Na}$) of $MoS_2@Sb_2S_3$/rGO superior to that of $Sb_2MoO_6$/rGO and $MoS_2@Sb_2S_3$, demonstrating that the 3D interconnected rGO network coated porous $MoS_2@Sb_2S_3$ heterostructure can accelerate $Na^+$ transport rate, thereby enhancing the electrochemical reaction kinetics.

Fig. 5g reveals the reason for the significantly improved sodium storage performance of $MoS_2@Sb_2S_3$/rGO composites. Firstly, the construction of the heterostructure of porous $MoS_2@Sb_2S_3$ sheet not only shortens the $Na^+$ diffusion distance, but also exposes more active sites. The different redox potentials of $MoS_2$ and $Sb_2S_3$ can also accommodate the huge volume changes during the process of sodiumization and desodiumization. Secondly, the two components $MoS_2$ and $Sb_2S_3$ will generate a phase boundary at the heterointerface, which will induce an internal electric field and accelerate the rapid transfer of $Na^+$ and electrons, enhancing the electrochemical reaction kinetics. Thirdly, the strong coupling between $MoS_2$ and $Sb_2S_3$ is beneficial to maintain the integrity of the Sb/$Na_2S$ interface and alleviate the agglomeration of nanoparticles, and thus form a stable SEI film. Finally, the external 3D interconnected rGO network provides a conductive framework with abundant 3D channels, which accelerates the $Na^+$ diffusion rate and facilitates the penetration of the electrolyte. Therefore, $MoS_2@Sb_2S_3$/rGO can exhibit high-rate capacity and ultra-long cycling life as an anode for SIBs.

In order to better explain the effect of heterostructure and graphene doping on the performance of composite materials, density functional theory (DFT) calculations were conducted [53–55]. Fig. 6(a-f) are the molecular model diagrams and three-dimensional differential charge density diagrams of the six structures of $Sb_2S_3$, Na-$Sb_2S_3$ $MoS_2@Sb_2S_3$, Na-$MoS_2@Sb_2S_3$, $MoS_2@Sb_2S_3$/rGO, and Na-$MoS_2@Sb_2S_3$/rGO, respectively, in which blue represents the increase of electron density, yellow represents the decrease of electron density. Fig. 6(g-l) are projected density of states (PDOS) diagrams of the six models. Comparing Fig. S14(a, d), it can be found that the surface electron orbital of $Sb_2S_3$ overlaps with the $Na^+$ electron orbital, forming a strong adsorption. It can be seen in Fig. 6(g, j) that the energy maximum of PDOS orbital after $Na^+$ adsorption rises from 25.07 eV to 27.63 eV, corresponding to the increase in the specific capacity of the anode electrode material after adsorbing $Na^+$ during the charging process, that is, the rise in the system's overall electron density. Comparing Fig. S14(d-f), it can be found that after combining $MoS_2$ on $Sb_2S_3$, the ability to adsorb $Na^+$ is weakened, which facilitates the release of $Na^+$ from the anode electrode material during discharge. The introduction of graphene provides

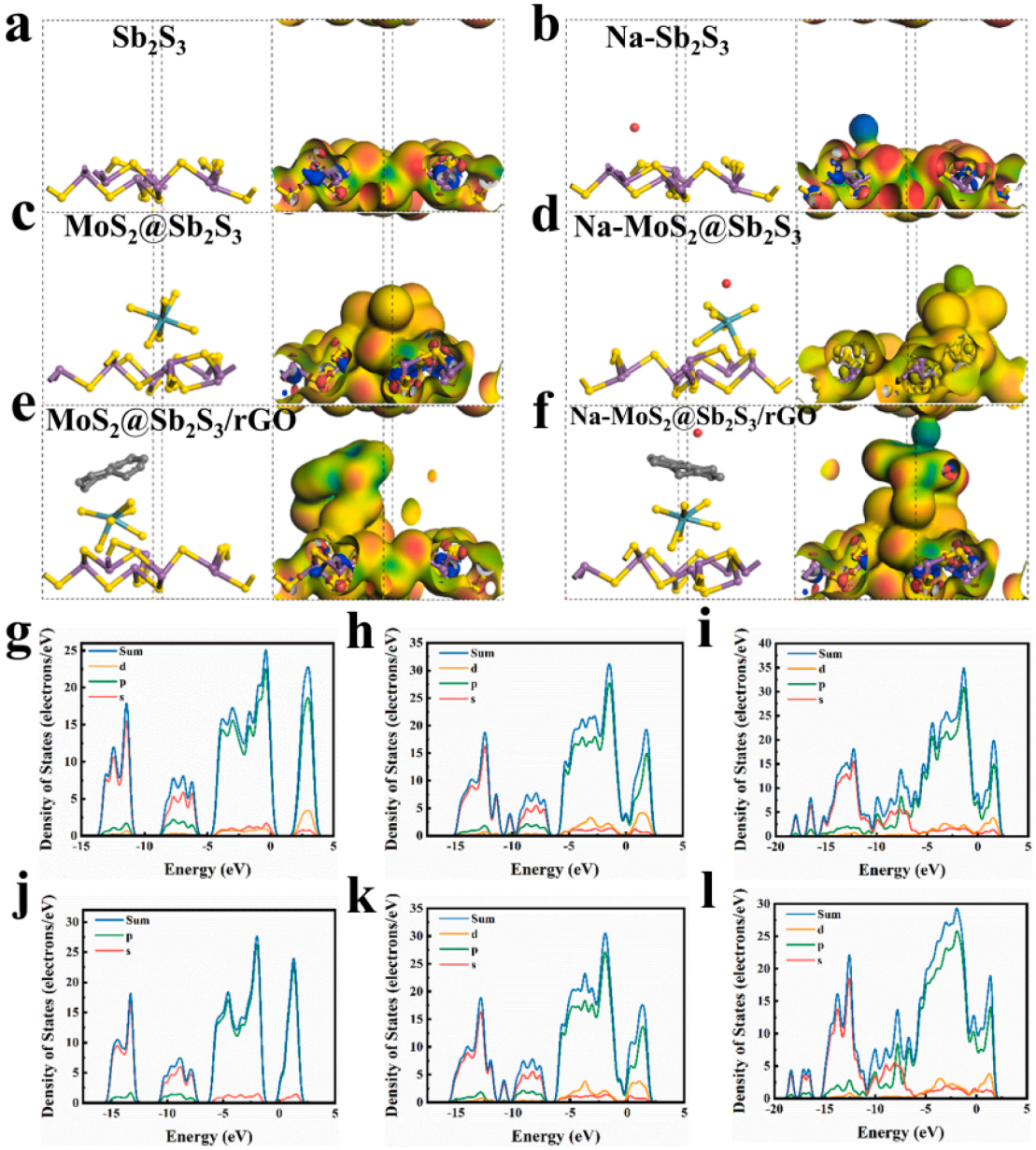


**Fig. 6.** Molecular models and 3D views of differential charge density for $Sb_2S_3$ (a), Na-$Sb_2S_3$ (b), $MoS_2$@$Sb_2S_3$ (c), Na-$MoS_2$@$Sb_2S_3$ (d), $MoS_2$@$Sb_2S_3$/rGO (e), Na-$MoS_2$@$Sb_2S_3$/rGO (f). Projected density of states (PDOS) for $Sb_2S_3$ (g), Na-$Sb_2S_3$ (j), $MoS_2$@$Sb_2S_3$ (h), Na-$MoS_2$@$Sb_2S_3$ (k), $MoS_2$@$Sb_2S_3$/rGO (i), Na-$MoS_2$@$Sb_2S_3$/rGO (l).

abundant electrons for the composite material, and the surrounding delocalized electron density increases, improving the conductivity of the anode material, which is consistent with the results in Fig. 5(e, f). The reason is that sp2 and sp3 in carbon materials are hybridized with a large number of loose electron clouds, which can effectively transport electrons. Comparing Fig. 6(g-i), it can be found that after $Sb_2S_3$ is compounded with $MoS_2$ and rGO, the bandgap at the top of the valence band and the bottom of the conduction band is filled, which increases the conductivity of the composite material.

In addition, the specific adsorption energy values for $Na^+$ were calculated. The adsorption energy of $Sb_2S_3$ to $Na^+$ is 10.34 eV, the adsorption energy of $MoS_2$@$Sb_2S_3$ to $Na^+$ is 3.03 eV, and the adsorption energy of $MoS_2$@$Sb_2S_3$/rGO to $Na^+$ is 0.529 eV. The huge interaction force between pure $Sb_2S_3$ and Na causes $Na^+$ to be firmly embedded in the $Sb_2S_3$ lattice, and it is difficult to come out during discharge, resulting in low coulombic efficiency. After the introduction of $MoS_2$ and rGO on the basis of $Sb_2S_3$, the adsorption capacity of $Na^+$ is weakened in turn, which facilitates the adsorption and deintercalation of $Na^+$, and improves the reaction reversibility and cycle stability of the composite material.

In Fig. S15(a, b), from the SEM images of $MoS_2$@$Sb_2S_3$/rGO composite after 100 cycles at 0.1 A $g^{-1}$, the porous nanosheet structure was well maintained without significant pulverization, indicating the excellent structural stability of the nanocomposite. Table S2 compares the present results with previous reports. While different reports based on different measurement conditions, it can be concluded that present $MoS_2$@$Sb_2S_3$/rGO composite as anode of SIBs achieved excellent performance specially in long-term cycle stability. At the same time, the $MoS_2$@$Sb_2S_3$/rGO composites exhibit competitive coulomb efficiencies (99 %, Fig. 4 d) compared with Sb and Mo based materials in Table S2. Its excellent electrochemical performance benefits from the new design of the three-dimensional interconnected conductive skeleton structure, which greatly shortens the $Na^+$ diffusion path and improves the conductivity and structural stability of the electrode material. Furthermore,

the formation of a heterostructure between $MoS_2$ and $Sb_2S_3$ facilitates the electron transfer kinetics and enhances the electrochemical performance of the composite.

## 4. Conclusion

In summary, the porous $MoS_2$@$Sb_2S_3$/rGO composite is prepared by hydrothermal and high-temperature sulfidation method for anode material of SIBs. The heterogeneous interface between $Sb_2S_3$ and $MoS_2$ can induce internal electric field, which promotes $Na^+$ pumping into the heterointerface and greatly reduces the activation barrier, thereby improving the whole material reaction kinetics. The $MoS_2$@$Sb_2S_3$ heterojunction is encapsulated in 3D interconnected rGO to form a conductive carbon framework. It provides certain mechanical toughness and higher specific surface area, buffering volume expansion during sodiumization and desodiumization, and providing 3D channels for the diffusion of $Na^+$. The different redox potentials of $MoS_2$ and $Sb_2S_3$ are beneficial to reduce composite material volume expansion and increase the cycle stability of the electrode material, manifested in a second-cycle discharge specific capacity of 591.6 mAh $g^{-1}$ at 5 A $g^{-1}$ and 162.1 mAh $g^{-1}$ after 1100 cycles. DFT calculation shows that a large delocalized electron density is formed around $MoS_2$@$Sb_2S_3$/rGO composite, which optimizes the electronic structure, increases the material's conductivity, facilitates the adsorption energy of the composite for $Na^+$, and promotes the reversibility of the electrochemical reaction.

## CRediT authorship contribution statement

**Ming Zhu:** Writing – original draft, Software. **Jialun Li:** Methodology, Conceptualization. **Xijia Yang:** Resources. **Xuesong Li:** Formal analysis. **Liying Wang:** Supervision. **Wei Lü:** .

## Declaration of Competing Interest

The authors declare that they have no known competing financial interests or personal relationships that could have appeared to influence the work reported in this paper.

## Data availability

Data will be made available on request.

## Acknowledgment

This work was supported by the National Natural Science Foundation of China (Grant No. 62004015 and 62004014) and the Department of Science and Technology of Jilin Province (Grant No. 20220101235JC, 20210101077JC and YDZJ202201ZYTS361).

## Appendix A. Supplementary material

Supplementary data to this article can be found online at https://doi.org/10.1016/j.apsusc.2023.157106.

## References

[1] Y.Q. Zhang, L. Tao, C. Xie, D. Wang, Y. Zou, R. Chen, Y. Wang, C. Jia, S. Wang, Defect Engineering on Electrode Materials for Rechargeable Batteries, Adv Mater. 32 (2020) e1905923.
[2] X.X. Zuo, J. Zhu, P. Müller-Buschbaum, Y.J. Cheng, Silicon based lithium-ion battery anodes: A chronicle perspective review, Nano Energy 31 (2017) 113–143.
[3] J.W. Xiang, Y. Wei, Y. Zhong, Y. Yang, H. Cheng, L.X. Yuan, H.H. Xu, Y.H. Huang, Building Practical High-Voltage Cathode Materials for Lithium-Ion Batteries, Adv. Mater. 111 (2022) 2200912.
[4] X.H. Zhang, Z. Li, L.G. Luo, Y. Fan, Z.Y. Du, A review on thermal management of lithium-ion batteries for electric vehicles, Energy 238 (2022), 121652.
[5] S. Sarkar, S. Roy, Y.F. Zhao, J.J. Zhang, Recent advances in semimetallic pnictogen (As, Sb, Bi) based anodes for sodium-ion batteries: Structural design, charge storage mechanisms, key challenges and perspectives, Nano Res. 14 (2021) 3690–3723.
[6] S. Dühnen, J. Betz, M. Kolek, R. Schmuch, M. Winter, T. Placke, Toward Green Battery Cells: Perspective on Materials and Technologies, Small Methods. 4 (2020) 2000039.
[7] S.S. Shi, C.L. Sun, X.P. Yin, L.Y. Shen, Q.H. Shi, K.N. Zhao, Y.F. Zhao, J.J. Zhang, FeP Quantum Dots Confined in Carbon-Nanotube-Grafted P-Doped Carbon Octahedra for High-Rate Sodium Storage and Full-Cell Applications, Adv. Funct. Mater. 30 (2020) 1909283.
[8] N.S. Muhammed Hafiz, G. Singla, P. Kumar Jha, Next generation sodium-ion battery: A replacement of lithium, Mater. Today:. Proc. (2022).
[9] X.D. Hu, X.H. Sun, S.J. Yoo, B. Evanko, F.R. Fan, S. Cai, C.M. Zheng, W.B. Hu, G. D. Stucky, Nitrogen-rich hierarchically porous carbon as a high-rate anode material with ultra-stable cyclability and high capacity for capacitive sodium-ion batteries, Nano Energy 56 (2019) 828–839.
[10] X. Ou, L. Cao, X. Liang, F. Zheng, H.-S. Zheng, X. Yang, J.-H. Wang, C. Yang, M. Liu, Fabrication of $SnS_2$/$Mn_2SnS_4$/carbon heterostructures for sodium-ion batteries with high initial coulombic efficiency and cycling stability, ACS Nano 13 (3) (2019) 3666–3676.
[11] Y.T. Wu, P. Nie, L.Y. Wu, H. Dou, X.G. Zhang, 2D MXene/$SnS_2$ composites as high-performance anodes for sodium ion batteries, Chem. Eng. J. 334 (2018) 932–938.
[12] M.K. Singh, J. Pati, D. Seth, J. Prasad, M. Agarwal, M.A. Haider, J.-K. Chang, R. S. Dhaka, Diffusion mechanism and electrochemical investigation of 1T phase Al-$MoS_2$@rGO nano-composite as a high-performance anode for sodium-ion batteries, Chem. Eng. J. 454 (2023), 140140.
[13] K. Li, L.u. Yue, J. Hu, X. Zhou, M. Xiao, C. Dai, C. Tian, Y. Yue, W. Zhang, J. Zhang, Construction of hollow core-shell $Sb_2S_3$/S@ S-doped C composite based on complexation reaction for high performance anode of sodium-ion batteries, Appl. Surf. Sci. 613 (2023) 156111.
[14] L. Cao, X.H. Liang, X. Ou, X.F. Yang, Y.Z. Li, C.H. Yang, Z. Lin, M.L. Liu, Heterointerface Engineering of Hierarchical $Bi_2S_3$/$MoS_2$ with Self-Generated Rich Phase Boundaries for Superior Sodium Storage Performance, Adv. Funct. Mater. 30 (2020) 1910732.
[15] H. Li, Y.Y. He, Y.X. Dai, Y.Q. Ren, T.T. Gao, G.W. Zhou, Bimetallic $SnS_2$/$NiS_2$@S-rGO nanocomposite with hierarchical flower-like architecture for superior high rate and ultra-stable half/full sodium-ion batteries, Chem. Eng. J. 427 (2022), 131784.
[16] K. Li, X.F. Liu, Y.C. Qin, Z.P. Zhao, Y.N. Xu, Y.H. Yi, H. Guan, Y.H. Fu, P. Liu, D. Li, $Sb_2S_3$-$Bi_2S_3$ microrods with the combined action of carbon encapsulation and rGO confinement for improving high cycle stability in sodium/potassium storage, Chem. Eng. J. 414 (2021), 128787.
[17] X. Xiong, G. Wang, Y. Lin, Y. Wang, X. Ou, F. Zheng, C. Yang, J.-H. Wang, M. Liu, Enhancing Sodium Ion Battery Performance by Strongly Binding Nanostructured $Sb_2S_3$ on Sulfur-Doped Graphene Sheets, ACS Nano 10 (12) (2016) 10953–10959.
[18] Z.Z. Pan, Y. Yan, N. Cui, J.C. Xie, Y.B. Zhang, W.S. Mu, C. Hao, Ionic Liquid-Assisted Preparation of $Sb_2S_3$/Reduced Graphene Oxide Nanocomposite for Sodium-Ion Batteries, Adv. Mater. Interfaces 5 (2018) 1701481.
[19] L.X. Zhang, F. Peng, M. Zhang, D. Li, Q.C. Pan, G.H. Yang, F.H. Zheng, Y.G. Huang, H.Q. Wang, Q.Y. Li, Heterostructured $FeS_2$/$SnS_2$ nanoparticles anchored on graphene for advanced lithium and sodium-ion batteries, Appl. Surf. Sci. 606 (2022), 154864.
[20] L.S. Cui, C.L. Tan, Q.C. Pan, Y.G. Huang, Y.H. Li, H.Q. Wang, F.H. Zheng, Q.Y. Li, SnS/$Fe_7S_8$ heterojunction embedded in three-dimensional N, S co-doped carbon nanosheets as anode material for sodium-ion batteries with long-term cycle life, Appl. Surf. Sci. 613 (2023), 155992.
[21] S. Dong, C. Li, X. Ge, Z. Li, X. Miao, L. Yin, ZnS-$Sb_2S_3$@C Core-Double Shell Polyhedron Structure Derived from Metal-Organic Framework as Anodes for High Performance Sodium Ion Batteries, ACS Nano 11 (6) (2017) 6474–6482.
[22] X. Luo, J. Shao, P. He, K. Li, W.W. Zhao, Construction of hierarchical ZnS/$MoS_2$ bimetallic sulfides heterostructures for high-performance sodium ion batteries, Appl. Surf. Sci. 607 (2023), 154821.
[23] L.B. Fang, Z.Y. Lan, W.H. Guan, P. Zhou, N. Bahlawane, W.P. Sun, Y.H. Lu, C. Liang, M. Yan, Y.Z. Jiang, Hetero-interface constructs ion reservoir to enhance conversion reaction kinetics for sodium/lithium storage, Energy Storage Mater. 18 (2019) 107–113.
[24] X.T. Li, H.J. Liang, X.L. Liu, R. Sun, Z.X. Qin, H.S. Fan, Y.F. Zhang, Ion-exchange strategy of $CoS_2$/$Sb_2S_3$ hetero-structured nanocrystals encapsulated into 3D interpenetrating dual-carbon framework for high-performance $Na^+$/$K^+$ batteries, Chem. Eng. J. 425 (2021), 130657.
[25] Y. Qin, Y. Zhang, J. Wang, J. Zhang, Y. Zhai, H. Wang, D. Li, Heterogeneous Structured $Bi_2S_3$/$MoS_2$@NC Nanoclusters: Exploring the Superior Rate Performance in Sodium/Potassium Ion Batteries, ACS Appl. Mater. Interfaces. 12 (2020) 42902–42910.
[26] S. Lu, J. Jiang, H. Yang, Y.-J. Zhang, D.-N. Pei, J.-J. Chen, Y. Yu, Phase Engineering of Iron-Cobalt Sulfides for Zn-Air and Na-Ion Batteries, ACS Nano 14 (8) (2020) 10438–10451.
[27] Y. Miao, X. Zhao, X. Wang, C. Ma, L.u. Cheng, G. Chen, H. Yue, L. Wang, D. Zhang, Flower-like $NiCo_2S_4$ nanosheets with high electrochemical performance for sodium-ion batteries, Nano Res. 13 (11) (2020) 3041–3047.
[28] G.J. Zhang, Y.D. Qu, F.H. Zhao, R.X. Dang, J. Yang, L.Y. Wang, Y.P. Zhang, L. F. Duan, Carbon-Interlayer $SnO_2$–$Sb_2O_3$ Composite Core-Shell Structure Anodes for Sodium-Ion Batteries, Front. Energy Res. 8 (2021), 606237.
[29] J.F. Li, W.X. Gao, L.Y. Huang, Y.C. Jiang, X.T. Chang, S.B. Sun, L.K. Pan, In situ formation of few-layered $MoS_2$@N-doped carbon network as high performance anode materials for sodium-ion batteries, Appl. Surf. Sci. 571 (2022), 151307.

[30] L.F. Duan, L.J. Zhao, H. Cong, X.Y. Zhang, W. Lü, C.L. Xue, Plasma Treatment for Nitrogen-Doped 3D Graphene Framework by a Conductive Matrix with Sulfur for High-Performance Li-S Batteries, Small. 15 (2019) e1804347.
[31] M. Ma, H. Wang, L. Xiong, S. Huang, X. Li, X. Du, Self-assembled homogeneous SiOC@C/graphene with three-dimensional lamellar structure enabling improved capacity and rate performances for lithium ion storage, Carbon 186 (2022) 273–281.
[32] G. Zhang, S. Zeng, L. Duan, X. Zhang, L. Wang, X. Yang, X. Li, W. Lü, The Dual Capacity Contribution Mechanism of SnSb-Anchored Nitrogen-Doped 3D Reduced Graphene Oxide Enhances the Performance of Sodium-Ion Batteries, ChemElectroChem 7 (22) (2020) 4663–4671.
[33] L. Cao, X. Gao, B. Zhang, X. Ou, J. Zhang, W.-B. Luo, Bimetallic Sulfide $Sb_2S_3$@$FeS_2$ Hollow Nanorods as High-Performance Anode Materials for Sodium-Ion Batteries, ACS Nano 14 (3) (2020) 3610–3620.
[34] S.F. Huang, M. Wang, P. Jia, B. Wang, J.J. Zhang, Y.F. Zhao, N-graphene motivated $SnO_2$@$SnS_2$ heterostructure quantum dots for high performance lithium/sodium storage, Energy Storage Mater. 20 (2019) 225–233.
[35] W. Ding, X.Z. Wu, Y.Y. Li, S. Wang, Z.C. Miao, P.F. Zhou, J. Zhou, S.P. Zhuo, Three-dimensional graphene-wrapped $Co_{0.85}Se$@C as high volumetric capacity anode material for lithium-ion batteries, Appl. Surf. Sci. 536 (2021), 147746.
[36] B.G. Choi, HoSeok Park, T.J. Park, M.H. Yang, J.S. Kim, S.-Y. Jang, N.S. Heo, S. Y. Lee, J. Kong, W.H. Hong, Solution chemistry of self-assembled graphene nanohybrids for high-performance flexible biosensors, ACS Nano 4 (5) (2010) 2910–2918.
[37] P.V. Prikhodchenko, J. Gun, S. Sladkevich, A.A. Mikhaylov, O. Lev, Y.Y. Tay, S. K. Batabyal, D.Y.W. Yu, Conversion of Hydroperoxoantimonate Coated Graphenes to $Sb_2S_3$@Graphene for a Superior Lithium Battery Anode, Chem. Mater. 24 (24) (2012) 4750–4757.
[38] S. Zhao, R.X. Jin, Y.B. Song, H. Zhang, S.D. House, J.C. Yang, R. Jin, Atomically precise gold nanoclusters accelerate hydrogen evolution over $MoS_2$ nanosheets: the dual interfacial effect, Small 13 (2017) 1701519.
[39] S. Wang, S. Liu, X. Li, C. Li, R. Zang, Z. Man, Y. Wu, P. Li, G. Wang, $SnS_2$ /$Sb_2S_3$ Heterostructures Anchored on Reduced Graphene Oxide Nanosheets with Superior Rate Capability for Sodium-Ion Batteries, Chemistry 24 (15) (2018) 3873–3881.
[40] G.M. Wang, X.X. Bi, H.L. Yue, R.C. Jin, Q.Y. Wang, S.M. Gao, J. Lu, Sacrificial template synthesis of hollow C@$MoS_2$@PPy nanocomposites as anodes for enhanced sodium storage performance, Nano Energy 60 (2019) 362–370.
[41] Y.B. Zhao, A. Manthiram, $Bi_{0.94}Sb_{1.06}S_3$ Nanorod Cluster Anodes for Sodium-Ion Batteries: Enhanced Reversibility by the Synergistic Effect of the $Bi_2S_3$–$Sb_2S_3$ Solid Solution, Chem. Mater. 27 (2015) 6139–6145.
[42] YangJie Liu, X. Hu, G. Zhong, J. Chen, H. Zhan, Z. Wen, Layer-by-layer stacked nanohybrids of N, S Co-doped carbon film modified atomic $MoS_2$ nanosheets for advanced sodium dual-ion batteries, J. Mater. Chem. A 7 (42) (2019) 24271–24280.
[43] D. Wang, L. Cao, D. Luo, R. Gao, H.B. Li, D.D. Wang, G.R. Sun, Z.Y. Zhao, N. Li, Y. T. Zhang, F. Du, M. Feng, Z.W. Chen, Chain mail heterostructured hydrangea-like binary metal sulfides for high efficiency sodium ion battery, Nano Energy 87 (2021), 106185.
[44] M. Deng, S. Li, W. Hong, Y. Jiang, W. Xu, H. Shuai, H. Li, W. Wang, H. Hou, X. Ji, Natural stibnite ore $Sb_2S_3$ embedded in sulfur-doped carbon sheets: enhanced electrochemical properties as anode for sodium ions storage, RSC Adv. 9 (2019) 15210–15216.
[45] Y. Li, R. Zhang, W. Zhou, X. Wu, H. Zhang, J. Zhang, Hierarchical $MoS_2$ Hollow Architectures with Abundant Mo Vacancies for Efficient Sodium Storage, ACS Nano 13 (5) (2019) 5533–5540.
[46] B.S. Reddy, M. Premasudha, K.-M. oh, N.S. Reddy, H.-J. Ahn, J.-H. Ahn, K.-K. Cho, Hydrothermal synthesis of $MoS_2$/rGO composite as sulfur hosts for room temperature sodium-sulfur batteries and its electrochemical properties, J. Storage Mater. 39 (2021), 102660.
[47] Y.Y. Zheng, L. He, X.R. Kong, Y. Song, Y. Zhao, Three-dimensional porous N-doped graphite carbon with embedded $CoS_2$ nanoparticles as advanced anode for sodium-ion batteries, Appl. Surf. Sci. 603 (2022), 154481.
[48] D.C. Zhao, Z. Zhang, J.H. Ren, Y.Y. Xu, X.Y. Xu, J. Zhou, F. Gao, H. Tang, S.P. Liu, Z.L. Wang, D. Wang, Y.T. Wu, X. Liu, Y. Zhang, $Fe_2VO_4$ nanoparticles on rGO as anode material for high-rate and durable lithium and sodium ion batteries, Chem. Eng. J. 451 (2023), 138882.
[49] A.-G. Nguyen, H.T.T. Le, R. Verma, D.-L. Vu, C.-J. Park, Boosting sodium-ion battery performance using an antimony nanoparticle self-embedded in a 3D nitrogen-doped carbon framework anode, Chem. Eng. J. 429 (2022), 132359.
[50] V. Augustyn, J. Come, M.A. Lowe, J.W. Kim, P.-L. Taberna, S.H. Tolbert, H. D. Abruña, P. Simon, B. Dunn, High-rate electrochemical energy storage through $Li^+$ intercalation pseudocapacitance, Nat Mater. 12 (6) (2013) 518–522.
[51] J. Wang, J. Polleux, J. Lim, B. Dunn, Pseudocapacitive contributions to electrochemical energy storage in $TiO_2$ (anatase) nanoparticles, J. Phys. Chem. C 111 (40) (2007) 14925–14931.
[52] W.S. Ma, J.W. Wang, H. Gao, J.Z. Niu, F.K. Luo, Z.Q. Peng, Z.H. Zhang, A mesoporous antimony-based nanocomposite for advanced sodium ion batteries, Energy Storage Mater. 13 (2018) 247–256.
[53] Y. Li, Z.H. Li, C. Zhou, X.B. Liao, X.W. Liu, X.F. Hong, X. Xu, Y. Zhao, L.Q. Mai, Gradient sulfur fixing separator with catalytic ability for stable lithium sulfur battery, Chem. Eng. J. 422 (2021), 130107.
[54] J. Lin, L. Yao, C. Zhang, H. Ding, Yuanhui, Wu, S. Li, J. Han, G. Yue, D. Peng, Construction of $Sb_2S_3$@SnS@C Tubular Heterostructures as High-Performance Anode Materials for Sodium-Ion Batteries, ACS Sustain. Chem. Eng. 9 (33) (2021) 11280–11289.
[55] B. Liang, N. Ma, Y. Wang, T. Wang, J. Fan, N-functionalized $Ti_2B$ MBene as high-performance anode materials for sodium-ion batteries: A DFT study, Appl. Surf. Sci. 599 (2022) 153927.